Analytic 1D Approximation of the Divertor Broadening S in the Divertor Region for Conductive Heat Transport

D. Nille, B. Sieglin, T. Eich, A. Scarabosio

Max Planck Institute for Plasma Physics, Boltzmannstr. 2, 85748 Garching, Germany

E-mail: Dirk.Nille@ipp.mpg.de

Abstract.

An analytic 1D approximation for the divertor broadening S is introduced, depending only on the electron temperature between X-point and target. It is compared to simulations solving the 2D heat diffusion equation, in order to describe the divertor broadening along a field line solely by the ratio of the perpendicular to the parallel diffusivities. By assuming the temperature dependence of these two diffusivities an integral form of S is derived for the area along the separatrix between X-point and target. Integration along the separatrix results in an approximation for S, being in agreement with the 2D simulations.

This approximation is furthermore compared to recent studies, which find a power law with negative exponent to describe S in terms of target temperature. This dependence is not reproduced in a pure conductive description, which instead shows a finite S for zero target temperature. This points to other mechanisms changing the shape of the heat flux profile – by additional widening or radiation losses – not included in the presented reduced approximation.

Keywords— Nuclear Fusion, Tokamak, Scrape-Off-Layer, Power Exhaust, Heat Transport, Divertor Broadening

1. Introduction

The description of the power load profile on the divertor targets relies on the knowledge of heat transport in the scrape-off layer (SOL), especially in the divertor volume. There the perpendicular transport into the private flux region (PFR) can significantly reduce the peak power load onto the divertor target [1, 2]. Recent studies show a scaling of the divertor broadening with a power law with negative exponent to the target electron temperature T_t, suggesting that lower T_t could distribute the power entering the divertor volume onto a larger surface area.

By describing the temperature dependence of the parallel and perpendicular heat transport an integral form of the divertor broadening S is derived, relying only on the electron temperature distribution along the separatrix between X-point and target. The results are in agreement with 2D simulations of diffusive transport and allow to discuss the benefit of a larger divertor broadening with respect to the effort needed to achieve lower target temperatures. Iterative numerical methods allow to use this approach for scenarios including heat losses between X-Point and divertor target, although this is not pursued in the work presented here.

Convective transport can not be neglected for high recycling conditions, hence the derived expression for S has to be treated with care.

Section 2 introduces a 1D approximation describing target heat load in experiments, and its connection to the parallel and perpendicular heat diffusivities for pure conductive transport. Section 3 introduces basic diffusion models used to describe the heat diffusion in the SOL. A scaling for S with the electron temperature is derived. Section 4 explains the 2D simulations used as reference for the analytic analysis presented in Section 5.

In Section 5 an analytic expression for S depending on the target temperature and target heat flux is derived. Neglecting other transport mechanisms – like convection, charge exchange or radiative losses – an expression for a *divertor averaged* temperature is given. The temperature dependence of S obtained by the 1D approximation is compared to 2D simulations.

Section 6 shows the authors interpretation of the introduced work.

Section 7 provides a summary and conclusions.

2. The Divertor Broadening S

To describe the heat flux density profile on the divertor target, a model assuming only diffusive parallel and perpendicular electron conduction is commonly used [3]. All temperatures and densities in this paper refer to the electrons, being the dominant species for parallel diffusive transport for comparable ion and electron temperatures, as seen in the Braginski equations [4]. For diffusive transport parallel to the field lines in the divertor volume the transport time

$$\tau_{\parallel} = \frac{L^2}{\chi_{\parallel}} \tag{1}$$

is an expression of connection length L – from the divertor entrance to the target – and parallel diffusivity $\chi_\parallel$. The parallel diffusion time is equivalent to the perpendicular diffusion time for heat entering the divertor region. The perpendicular diffusion length is thus given by

$$S = \sqrt{\tau_\parallel \cdot \chi_\perp} = L\sqrt{\frac{\chi_\perp}{\chi_\parallel}} \tag{2}$$

and is further called divertor broadening. Measurements of the heat flux profiles in tokamaks like ASDEX Upgrade (AUG) in Garching and JET in Culham are done by infrared thermography in target coordinates called s with separatrix position s_0. Quantities following the magnetic field lines can be related to the outer midplane, to the radial coordinate called x, for comparison between different magnetic geometries and machines. The coordinates are correlated by the effective flux expansion $f_{x,eff} = f_{x,magn} \cdot f_{x,geom}$, which is the product of the magnetic flux expansion f_x^{mag} and poloidal inclination of the tile with respect to the field lines. The position mapped to the outer mid plane is then

$$x = \frac{s - s_0}{f_x} \tag{3}$$

with $x = 0$ representing the separatrix. For perpendicular transport being described as 1D diffusion, a power density profile given by a delta peak entering the divertor area is spread to a Gaussian of width S when reaching the target without flux expansion. The measure on the target is $S_{tar} = S \cdot f_x$. In this work S refers to the divertor broadening mapped to the outer midplane if not marked otherwise.

Note that the poloidal inclination between field lines and target is not included in this discussion, as it is only a mapping from parallel heat flux along the plasma onto what is seen as perpendicular heat flux of the target material. For the sheath condition this angle, which is machine and configuration dependent, has to be included. This work focuses on the parallel transport in the plasma and therefore omits this angle.

The X-point heat flux density profile is described [5] by an exponential with peak value q_0 at the separatrix and decay length λ_q at the midplane with the radial coordinate x:

$$q(x) = q_0 \cdot \exp\left(-\frac{x}{\lambda_q}\right) : x > 0\ . \tag{4}$$

Following the simplified model for perpendicular diffusion, the target heat flux profile is described by the X-point profile convolved with a Gaussian of width S, representing the broadening in the divertor region:

$$q_\parallel(s) = \frac{q_0}{2} \exp\left(\left(\frac{S}{2\lambda_q}\right)^2 - \left(\frac{s - s_0}{f_x \lambda_q}\right)\right) \cdot \operatorname{erfc}\left(\frac{S}{2\lambda_q} - \frac{s - s_0}{f_x S}\right)\ . \tag{5}$$

Figure 1 shows the flattening of the heat flux density profile from the raw exponential in deep red – starting at the strike point at $s_0 = 0$ – up to a value of $S = 10\,\mathrm{mm}$ in green in steps of 1 mm for S, keeping $\lambda_q = 3\,\mathrm{mm}$ and $q_0 = 10\,\mathrm{MW\,m^{-2}}$ fixed.

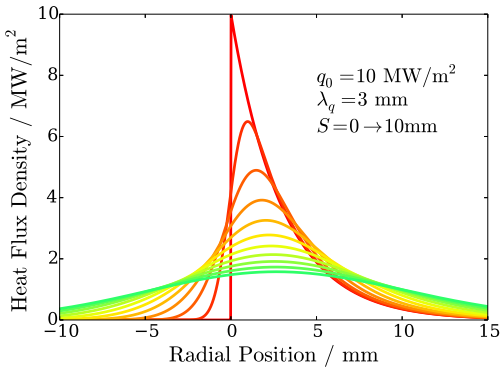

Figure 1. Influence of divertor broadening S: Target heat flux profiles with steps of 1 mm in the the divertor broadening S, starting from the unperturbed X-point distribution in red up to $S = 10$ mm in green.

The peak heat flux $\hat{q}$ onto the target is used as design parameter and correlated to the integrated power profile of arbitrary shape $q(s)$ onto the target element by the integral power decay length

$$\lambda_{int} \equiv \int \frac{q(s)}{\hat{q}} \mathrm{d}s \ . \tag{6}$$

The benefit of an additional divertor broadening S on λ_{int} compared to an exponential with decay length λ_q – as described in (5) – is approximated [5] by:

$$\lambda_{int} \simeq \lambda_q + 1.64 \cdot S \ . \tag{7}$$

Studies predict a value for the heat decay length of about $\lambda_q \approx 1$ mm for future fusion relevant machines like ITER, which is smaller than for current machines like AUG and JET [3]. Therefore the divertor broadening gains importance to meet the material limits of the divertor target with respect to the incoming heat flux density. Scaling laws for S are available for AUG [6, 2], investigating S for target electron temperatures above 20 eV. Below this temperature, the increasing radiation prohibits IR measurements in AUG to deduce S. A study including simulations done in SOLPS [1, 7, 8] shows a scaling inverse to the target electron temperature. This will be further discussed in Section 7.

The analysis on S in this work is based on the transport model introduced in section 3 and is aimed to find a description for the divertor broadening with respect to the temperature distribution in the divertor volume. Intent is to quantify discrepancies in simulations and experiments for a better understanding of the transport mechanisms including a variety of particle and heat transport processes.

3. Diffusion Models

Heat transport parallel to the magnetic field in the SOL is described by Spitzer-Härm conduction [9] with the conductivity

$$\kappa_{\parallel} = \kappa_{\parallel,0} T^{5/2}. \tag{8}$$

The factor $\kappa_{\parallel,0} \simeq 2000\,\mathrm{W\,m^{-1}\,eV^{-7/2}}$ is a valid approximation for machines like AUG and JET for $Z_{eff} \approx 1.3$ [4]. The diffusivity is connected to the conductivity by the density [10]

$$\chi = \frac{\kappa}{\rho c_p} \propto \frac{\kappa}{n} \,. \tag{9}$$

As only the ratio of the diffusivities – perpendicular versus parallel - is of interest, the factor representing the degrees of freedom of an electron in c_p is not relevant in this work. Therefore the parallel diffusivity is given as

$$\chi_\parallel = \frac{\kappa_{\parallel,0}}{n_e} T^{5/2} \,. \tag{10}$$

In the further calculations the exponent on the temperature is referred to as β, with the value 5/2 for parallel electron conduction. Transport perpendicular to the magnetic field is characterised by a Spitzer-Härm like conductivity for this work, with the temperature dependence expressed by the exponent α:

$$\chi_\perp^{SH} = \frac{\kappa_{\perp,0}^{SH}}{n_e} \cdot T^\alpha \tag{11}$$

Note that with this definition the density dependence in the ratio of the diffusivities cancels. Bohm described the perpendicular diffusion coefficient [11] in arc discharges as

$$\chi^B = \frac{1}{16}\frac{T}{eB} = \kappa_\perp^B \cdot T \tag{12}$$

being not dependent on n_e but on B, as suggested by recent experiments at AUG [2]. Bohm like diffusion in this work uses the modified form

$$\chi_\perp^B = \kappa_\perp^B \cdot T^{\alpha'} \tag{13}$$

with the exponent α' being related to α in (11) by

$$\alpha' = \alpha + 1 \,. \tag{14}$$

Neglecting the dependency on the total magnetic field, we find a perpendicular diffusion coefficient scaling linearly with T. Using Bohm diffusion to describe perpendicular transport, the density dependence of the parallel diffusivity remains in the ratio of the diffusivities. To eliminate this explicit dependency on the density, the ideal gas law $p = nT \rightarrow 1 = \frac{nT}{p}$ is used. It allows to include the density dependence implicitly in the temperature component for a given pressure:

$$\begin{aligned}
\chi_\perp^{SH} &= \kappa_{\perp,0}^{SH}\frac{T^\alpha}{n} \\
&= \kappa_{\perp,0}^{SH}\frac{T^\alpha}{n} \cdot \frac{nT}{p} \\
&= \kappa_{\perp,0}^{SH}\frac{T^{\alpha+1}}{p} \\
&= \kappa_{\perp,0}^{SH} T^{\alpha'}/p \\
&\propto \chi_\perp^B/p
\end{aligned} \tag{15}$$

For clearification: α is the exponent for the temperature dependence of a Spitzer-Härm-like perpendicular diffusion coefficient, α' for Bohm-like diffusion with an additional $\frac{1}{p}$. For example $\alpha = 0$ corresponds to Spitzer-Härm-like transport with T^0 and $1/n$ scaling or Bohm-like transport with T^1 ($\alpha' = \alpha + 1 = 1$) and no density dependence. Also note, that here $\kappa_\perp$ is treated as some constant factor. The absolute values depend on the chosen model and implicitly on the plasma parameters like the effective charge.

Of interest is furthermore how S scales with temperature and pressure. For Spitzer-Härm-like transport we find

$$S^{SH} \propto \sqrt{\frac{\kappa_{\perp,0}^{SH}/n}{\kappa_{\parallel,0}/n}} \cdot \sqrt{\frac{T^\alpha}{T^\beta}} \propto T^{\frac{\alpha-\beta}{2}} \tag{16}$$

which leaves a scaling with temperature and a constant exponent. For Bohm-like transport we find

$$S^B \propto \sqrt{\frac{\kappa_{\perp,0}^{B}}{\kappa_{\parallel,0}/n}} \cdot \sqrt{\frac{T^{\alpha'}}{T^\beta}} = \sqrt{\frac{\kappa_{\perp,0}^{B}}{\kappa_{\parallel,0}/n}} \cdot \sqrt{\frac{p}{nT}} \cdot \sqrt{\frac{T^{\alpha'}}{T^\beta}} \propto \sqrt{p}\, T^{\frac{\alpha-\beta}{2}} \tag{17}$$

with a temperature exponent similar to Spitzer-Härm-like transport, but with an additional pressure dependence.

Including the density implicitly into the temperature is correct for analysing a single field line for which pressure conservation holds. For a non-homogeneous pressure, S scales with the square root of the pressure. Recent studies suggest a scaling of S with about the square root of the divertor density [2]. This indicates a weak or no density dependence of $\chi_\perp$, given the experimental uncertainty. The formulation where the density is treated implicitly in the temperature assuming a negligible influence of the pressure – by pressure conservation or a minor impact due to the weak scaling – is used in the 1D approximation. For Bohm-like perpendicular transport in equation (17) this corresponds to $\alpha' = 1$. In equation (16) for Spitzer-Härm like transport it corresponds to $\alpha' = 0$. Therefore the plots in section 5.2 show result with $\alpha = 0$. The agreement between 1D approximation and 2D model is independent of the actual value of α.

Other numerical tools used to study the heat and particle transport in the SOL are using similar, but not necessarily the same expressions and approximations for the diffusion coefficients. For the SOLPS runs in [1] a constant perpendicular diffusivity throughout the entire SOL is used.

4. Simulation of 2D Heat Diffusion Equation

As reference for the 1D analysis a 2D model in slab geometry is used, solving the heat diffusion equation in the SOL. For parallel transport Spitzer-Härm conduction is assumed. For perpendicular transport a Spitzer-Härm like diffusivity as described in section 3 with a fixed temperature exponent α and inverse density dependence is used. Operator splitting [12] is used to separate the parallel and perpendicular transport,

solving them independently. The following derivation is valid for the resulting 1D or any isotropic case and any integrable $\kappa(T)$.

The heat diffusion equation

$$\frac{\partial T}{\partial t}\rho c_p = \nabla \cdot (\kappa(T)\nabla T) \tag{18}$$

with mass density ρ and specific heat capacity c_p is solved using the heat potential

$$u(\kappa) = \int_0^T \kappa(T')dT' \,. \tag{19}$$

For the heat potential the first partial derivative in space is

$$\frac{\partial u}{\partial x} = \frac{\partial u}{\partial T}\frac{\partial T}{\partial x} = \kappa\frac{\partial T}{\partial x} \tag{20}$$

and the second spatial derivative denoted with the Laplace-operator $\nabla^2 = \nabla \cdot \nabla$

$$\nabla^2 u = \nabla \cdot (\kappa \nabla T) \tag{21}$$

and the partial derivative in time

$$\frac{\partial u}{\partial t} = \frac{\partial u}{\partial T}\frac{\partial T}{\partial t} = \kappa\frac{\partial T}{\partial t} \,. \tag{22}$$

This substitution leads to the semi-linear differential equation

$$\frac{\partial u}{\partial t} = \frac{\kappa}{\rho c_p}\nabla^2 u = \chi \nabla^2 u \tag{23}$$

instead of the non-linear second order partial differential equation (18). An alternate direction implicit Crank-Nicolson scheme [12] is implemented to solve the heat diffusion equation. Inlcuding operator splitting leads to

$$\frac{\partial u}{\partial t} = \left(\partial_\parallel \chi_\parallel + \partial_\perp \chi_\perp\right) u \,. \tag{24}$$

The parallel and perpendicular term are solved sequentially, leading to two 1D equation to be solved for a single time step.

The results shown in section 5 of the 1D approximation use pressure conservation. For direct comparison the 2D model uses a homogeneous pressure distribution in the divertor region. Furthermore the presented 2D results are obtained by setting the target temperature to a fixed value. For comparison less constrained simulations were performed, with the target electron temperature obeying the sheath heat flux criteria for target density distributions obtained from experiments. The obtained values for S in these refined simulations are up to 25% larger compared to the simple system. The former one can therefore be seen as pessimistic approach to evaluate the divertor broadening S. It should be noted, that the sheath boundary at the target effectively prevents low peak target temperatures without changing involved parameters like q_0 or L significantly. Loss terms like radiation, charge exchange, etc. can lead to target temperatures $< 5\,\mathrm{eV}$. This can be taken into account in the 1D approximation, where a numerical solution only depends on the temperature and density profiles along the separatrix.

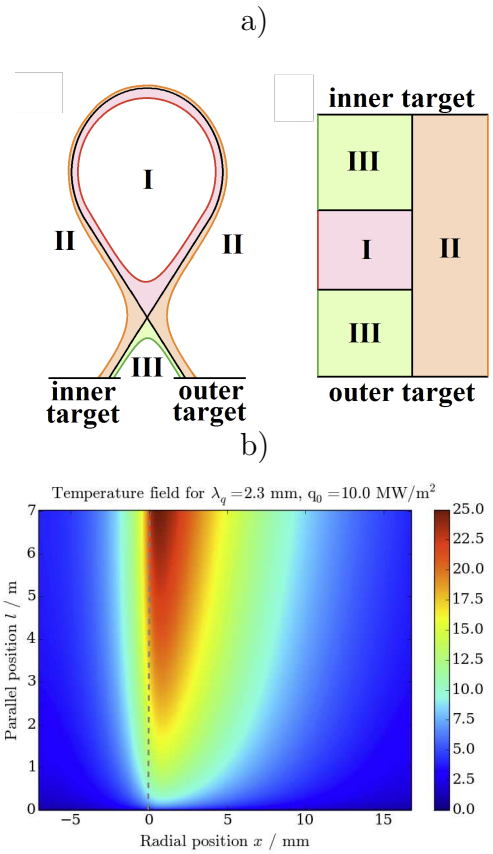

Figure 2. a) Sketch of the poloidal cross section of a tokamak on the left. On the right a sketch of the slab geometry showing the mapping of the regions: I) Confined area, II) SOL, III) PFR. b) Example of the electron temperature distribution in eV resulting from a 2D simulation, restricted to the divertor region. The vertical dashed line marks the separatrix.

4.1. Geometric Configurations and Boundary Conditions

The numerical tool is able to solve the 2D heat diffusion equation in various topologies. Figure 2 shows a comparison between a) the structure of the slab geometry and b) the computational grid with a steady state temperature field. The numerical tool can include the SOL above the X-point, but for studying S for given X-point conditions only the divertor region is included. This is called the divertor configuration. The divertor target is at the bottom, the divertor entrance at the top and the separatrix is marked with a vertical line. As the diffusive model is not describing the transport in the confined region, it is excluded from the computational domain. For the example shown the length of the divertor leg is set to $L = 7\,\mathrm{m}$ – based on AUG. A single connection length for all radii is assumed.

The lateral boundary conditions – following the innermost and outermost field line – at the sides of the computational domain describe no heat transfer through the boundary ($q_\perp \propto \partial_\perp T = 0$). The perturbation of these boundaries to the parallel and perpendicular heat flux is negligible for a sufficient width of the domain. Several radial decay length

of the parallel heat flux λ_q and from the 1D approximation S_{1D} are are used, defining the widths width respect to the separatrix for the SOL

$$w_{SOL} = \sqrt{(3.5S_{1D})^2 + (7\lambda_q)^2} \tag{25}$$

and the width from the separatrix for the PFR

$$w_{PFR} = \sqrt{(5S_{1D})^2 + (2\lambda_q)^2}\,. \tag{26}$$

The expected S_{1D} is obtained using the 1D approximation introduced in section 5, while λ_q is a given value for a specific simulation.

The boundary condition at the X-point is set to a given parallel heat flux profile. The parameters q_0 and λ_q define the profile entirely.

At the target, the boundary condition is given by a fixed temperature.

In addition, to mimic the behaviour of the sheath, the temperature in front of the target is adjusted according to a scaling taking into account the heat flux impinging from the plasma. It is based on the sheath theory [13] describing the heat flux in the sheath

$$q_{sh} = \Gamma_e \gamma T_e \tag{27}$$

by the electron particle flux Γ_e, the electron temperature T_e and the heat transmission factor γ at the sheath entrance. This equation holds for the same ion and electron values $\Gamma_i = \Gamma_e$ and $T_i = T_e$ and the total heat transmission factor $\gamma = \gamma_e + \gamma_i$. According to the Bohm criterion the speed of incoming particles v is at least as large as the plasma sound speed c

$$v \geq c \approx \sqrt{\frac{T_e}{m_i}}\,. \tag{28}$$

For determining the sound speed the contribution from the ions is neglected. The resulting particles flux – assuming $v = c$ – is then

$$\Gamma_e = c n_e \tag{29}$$

with the electron density n_e. The heat flux transferred through the sheath – using again $T \cdot n = p$ – is approximated with

$$q_{sh} \approx \frac{T_e^{3/2}}{\sqrt{m_i}}\, n_e \gamma \;=\; T_e^{1/2} p \frac{\gamma}{\sqrt{m_i}} \;\propto T_e^{1/2} p\,. \tag{30}$$

Solving for the temperature we find the temperature where the sheath conducts a given heat flux density to the target:

$$T_{sh} = \frac{q_{sh}^2}{p^2} \cdot \frac{m_i}{\gamma^2} \;\propto \left(\frac{q_s h}{p}\right)^2\,. \tag{31}$$

From the two grid cells closest to the target boundary the parallel heat flux impinging onto the sheath is calculated. This heat flux is used as q_S in equation (31) to determine

the temperature T_S. The boundary – the target temperature distribution – is updated iteratively to find the global solution for given upstream parameter. Simulations, not presented in this work, with this boundary condition were performed, showing similar heat flux distributions. For peak temperatures, resulting from the sheath-boundary, being comparable to the constant preset target temperature, the profile shape and deduced parameters are not altered significantly. For the comparison in section 5.2 and the temperature scan to determine the behaviour of S the fixed temperature boundary condition is used.

The resulting target heat flux density profiles do not depend strongly on the parallel heat flux density q_0. As the computational time for convergence depends on the time step, which is limited by the largest diffusivity, larger parameter scans were performed for rather low parallel heat flux densities $q_0 \approx 1\,\mathrm{MW\,m^{-2}} - -10\,\mathrm{MW\,m^{-2}}$. Reason is the scaling of the parallel conductivity with $T^{5/2}$, being the limiting factor for the time step. Simulations for higher values like $q_0 = 1000\,\mathrm{MW\,m^{-2}}$ were performed to confirm the trends found for lower values. The contribution of this high-temperature area to the target profile is however small, as presented in this work.

5. 1D Approximation of S

Equation (2) $\left(S \approx L\sqrt{\frac{\chi_\perp}{\chi_\parallel}}\right)$ – in which the diffusivities resemble averaged values – can be interpreted as result of the spatial integral parallel to the magnetic field

$$S = \int_0^L \sqrt{\frac{\chi_\perp}{\chi_\parallel}}\mathrm{d}l \; . \tag{32}$$

With Spitzer-Härm conduction parallel (10) and Spitzer-Härm like conduction perpendicular (11) to the magnetic field we find

$$S = \sqrt{\frac{\chi_{\perp,0}}{\chi_{\parallel,0}}}\int_0^L T(l)^{\frac{\alpha-\beta}{2}}\mathrm{d}l = \sqrt{\frac{\kappa_{\perp,0}}{\kappa_{\parallel,0}}}\int_0^L T(l)^{\frac{\alpha-\beta}{2}}\mathrm{d}l \; . \tag{33}$$

For a remaining density dependence the substitution leading to (17) can be used, changing the α in the exponent to $\alpha' = \alpha - 1$ and adding $\sqrt{p}$ to the temperature term

$$S = \sqrt{\frac{\chi_{\perp,0}}{\chi_{\parallel,0}}}\int_0^L \sqrt{p}\cdot T(l)^{\frac{\alpha'-\beta}{2}}\mathrm{d}l \; .$$

Assuming pressure conservation – or negligible changes in $\sqrt{p}$ – leads to the same form of the integral as in (33).
For the rest of this section the Spitzer-Härm like perpendicular transport model ($\chi_\perp \propto 1/n$) and equation (33) is used.

Assuming a constant parallel heat flux $q_\parallel$ – implying no volume radiation and $S \ll \lambda_q$ – the temperature profile along the magnetic field is described by the two point model:

$$T(l) = \left(T_t^{\beta+1} + (\beta+1)\frac{q_\parallel \cdot l}{\kappa_{\parallel,0}}\right)^{1/(\beta+1)} \; . \tag{34}$$

The plasma temperature along a field line depends on the target electron temperature T_t and distance l from the target. For zero target temperature ($T_t = 0$) the temperature at the X-point ($l = L$) is denoted as

$$T_{X,0} = \left((\beta + 1) \frac{q_\parallel \cdot L}{\kappa_{\parallel,0}} \right)^{1/(\beta+1)} . \tag{35}$$

With this expression equation (34) is rewritten as

$$T(l) = \left(T_t^{\beta+1} + T_{X,0}^{\beta+1} \frac{l}{L} \right)^{1/(\beta+1)} . \tag{36}$$

Equation (32) is expressed by using the derived term for $T(l)$ containing l explicitly in the integral:

$$S = \sqrt{\frac{\chi_{\perp,0}}{\chi_{\parallel,0}}} \cdot \int_0^L \left(T_t^{\beta+1} + T_{X,0}^{\beta+1} \cdot \frac{l}{L} \right)^{\frac{\alpha-\beta}{2(\beta+1)}} \mathrm{d}l \tag{37}$$

Note that the exponent $\frac{\alpha-\beta}{2(\beta+1)}$ is negative for experimental relevant SOL transport. For $-1 \leq \alpha \leq +1$ the exponent is in the range of -0.5 to -0.2 . As a result the integral does not diverge when the integrand reaches zero.
The solution to the integral is

$$S = L \cdot \sqrt{\frac{\chi_{\perp,0}}{\chi_{\parallel,0}}} \cdot \frac{2(\beta+1)}{\alpha+\beta+2} \cdot \frac{\left(T_t^{\beta+1} + T_{X,0}^{\beta+1} \right)^{\frac{\alpha+\beta+2}{2(\beta+1)}} - T_t^{\frac{\alpha+\beta+2}{2}}}{T_{X,0}^{\beta+1}} \tag{38}$$

and expresses S by $T_{X,0}$ – given by $q_\parallel$ and L – and T_t, which are measurable quantities in the experiment.

In the case $T_t = 0$ the result simplifies to

$$S = L \sqrt{\frac{\chi_{\perp,0}}{\chi_{\parallel,0}}} T_{X,0}^{-\frac{\beta-\alpha}{2}} \cdot \frac{2(\beta+1)}{\alpha+\beta+2} . \tag{39}$$

This finite value is scaling inverse with the temperature at the X-point and with the square root of the ratio of the temperature independent diffusivity factors. The term

$$\frac{2(\beta+1)}{\alpha+\beta+2} = \text{const} \tag{40}$$

is identified as a constant factor for a given transport model. A temperature dependent expression similar to equation (2) is found after defining the effective divertor temperature for S

$$T_S = T_{X,0} \cdot \left(\frac{2(\beta+1)}{\alpha+\beta+2} \right)^{-\frac{2}{\beta-\alpha}} . \tag{41}$$

Substituting the two last terms in equation (39) for (41) with the right exponent yields

$$S \approx L \cdot \sqrt{\frac{\chi_\perp}{\chi_\parallel}} = L \cdot \sqrt{\frac{\chi_{\perp,0}}{\chi_{\parallel,0}}} T_S^{-\frac{\beta-\alpha}{2}} . \tag{42}$$

Note the explicit linear dependence on the connection length to the X-point and the inverse scaling with the averaged temperature. As the connection length is increased – assuming the target temperature stays constant – the effective temperature T_S increases. As a result the divertor broadening is increasing less than linear with the divertor length. A decrease in the target temperature – when it is significantly lower than the X-point temperature – has little influence on S, as the relevant temperature is dominated by $T_{X,0}$ and scales only weak with the target temperature.

For a non-constant $q_\parallel(l)$, for example lowered due to the perpendicular diffusion, the integral is iterated numerically to find S for given q_0 and T_t. This approach also allows to take losses, e.g. due to radiation or charge exchange, into account. From discrete temperature and density profiles – say from numerical solvers like SOLPS – S can be evaluated by summing over the ratio of the transport times the finite parallel path

$$\Delta S = \sqrt{\frac{\chi_\perp}{\chi_\parallel}} \cdot \Delta l \tag{43}$$

$$S = \sum_0^N \Delta S \tag{44}$$

starting with $S = 0$ at the divertor entrance.

Figure 3 shows the resulting value of T_S for given T_t for connection length $L = 7\,\mathrm{m}$, $\alpha = 1$ and three parallel heat flux densities. For this comparison the heat flux density q_0 is assumed to be constant along the field line to be independent of the actual broadening, giving an upper boundary. Note that the target heat flux densities are obtained from the parallel heat flux density in the plasma approaching the target by taking the field line inclination angle and the geometric flux expansion into account. The higher the target temperature, the closer is the effective temperature to the target value, as the parallel temperature gradient decreases for increasing temperature for the same heat flux density.
Figure 4 shows the divertor broadening relative to the value of S at $T_t = 0$. The decrease of S depends on the parallel heat flux density, which is like in figure 3 kept constant. This graph shows, that the analysis of S with the target temperature as reference is expected to depend on the parallel heat flux density q_0.

5.1. Approaches to $q(l)$

Taking the divertor broadening in the 1D approximation into account, the question how to calculate $q(l)$ arises. By definition q_0 is the peak heat flux at the divertor entrance. A decrease of the parallel heat flux density along the divertor volume reduces the parallel temperature gradient. A pessimistic approach is to use the peak heat flux according to the integral decay length (6) as S increases along the divertor leg:

$$q(l) = q_0 \cdot \frac{\lambda_q}{\lambda_q + 1.64 S(l)} \,. \tag{45}$$

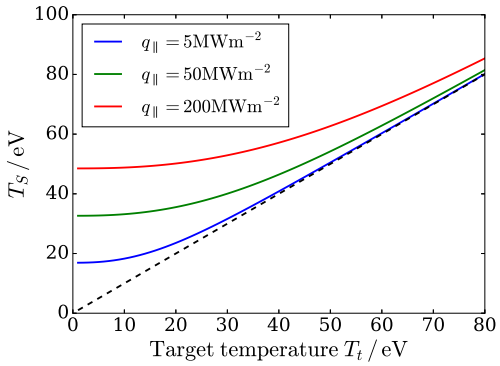

Figure 3. Effective divertor broadening temperature T_S for varying target temperature T_t for different parallel heat flux densities. The effective divertor temperature T_S is scaling linearly to the target temperature for very high temperatures, where there is virtually no gradient along the field line. For low temperatures, T_S clearly stagnates and with it S.

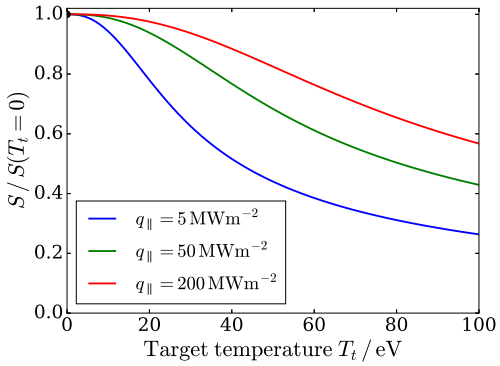

Figure 4. Divertor broadening relative to $S(T_t = 0)$ for varying target temperature and three different parallel heat flux densities.

This approach is pessimistic, as the radial position of the peak heat flux is moving into the SOL as the heat flux profile degrades by perpendicular transport. Using the peak heat flux independent of its radial position leads to the steepest parallel temperature gradient and therefore to an upper limit of the temperature evolution along the field lines near the separatrix. As this is a robust method, it is used for the evaluation in the next section.

A less pessimistic approach is to use the temperature profile along a single field line, located in the SOL. Therefore equation (5) can be evaluated with $S(l)$. The issue is the dependence of the result on the chosen distance to the separatrix. For values much smaller than the divertor broadening $x \ll S$ the parallel heat flux density drops quickly after the X-point, due to the perpendicular transport into the PFR. For $x \approx S$ the parallel profile $q(l)$ approaches the shape of the pessimistic method described before this method, but stays below q_0 at the divertor entrance. Due to the drawback of the

shape dependence it is not feasible to use q at a fixed radial distance to the separatrix.

5.2. Comparison to 2D Calculation and Experiment

The heat flux profiles from 2D simulation were compared to experimental data and reproduce the shape for same λ_q and S, with the fit-function (5) as reference. Figure 5 shows an example of a measure profile for an L-Mode example and figure 6 a result of the simulation for a similar profile. The resemblance includes a systematic deviation, where the decay into the PFR is is predicted steeper by the fit than it is the data. This deviation is also observed in some SOLPS results.

The experimental reference data are from a low-power – 0.8 MW ECRH – and low-density – $n_e \approx 1.5 \times 10^{19}\,\mathrm{m}^{-3}$ – L-Mode which yields the cleanest heat flux density profiles. The target heat flux density – measured perpendicular to the surface – $q_{0,target} \approx 0.7\,\mathrm{MW\,m^{-2}}$ corresponds to about $q_0 = 15\,\mathrm{MW\,m^{-2}}$ parallel heat flux in the plasma. The agreement between 1D approximation and 2D simulation remains for higher heat flux values.

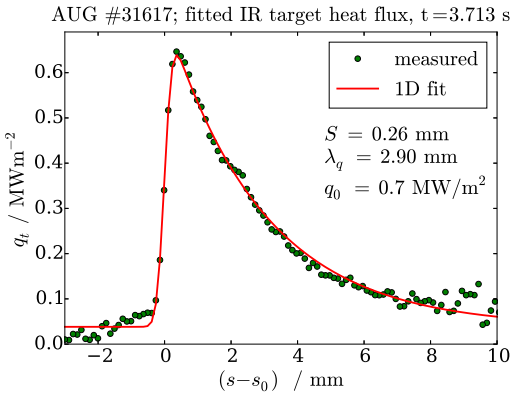

Figure 5. Divertor heat flux profile deduced from IR-Data in AUG. The target position is divided by the flux expansion, corresponding to a mapping to the outer midplane.

Figure 7 shows the variation of peak parallel heat flux, temperature and divertor broadening S along the separatrix between X-point and target. On the left hand side is the divertor entrance, with $S \equiv 0$ and $q(l) = q_0$, as the first and second boundary conditions. The temperature at the target – on the right hand side for $L = 7\,\mathrm{m}$ is set as the third boundary condition and the result determined numerically to obey the constraints at both sides. Boundary conditions are $q_0 = 10\,\mathrm{MW\,m^{-2}}$, $S_t = 1\,\mathrm{mm}$ and $T_t = 10\,\mathrm{eV}$. The gradient of $S(l)$ is highest near the target, as the falling temperature reduces the parallel transport compared to the perpendicular transport. A linear increase of $S \propto l$ can be a reasonable approximation for 1D models taking the parallel heat flux density in the divertor volume into account, without treating the broadening mechanism. Figure 8 shows a comparison between the parallel heat flux density close to the separatrix in the SOL (sep), in the SOL and in the PFR. Relevant parameters are

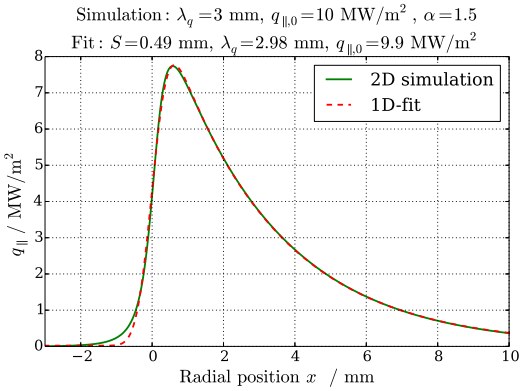

Figure 6. Divertor heat flux profile from the 2D simulation in divertor geometry with λ_q and q_0 similar to the profile in 5.

$q_0 = 1\,\mathrm{MW\,m^{-2}}$, $\lambda_q = 1\,\mathrm{mm}$, $S \approx 0.99\,\mathrm{mm}$. The deviation of the profiles at the target is due to a mismatch between the target heat flux profile and the 1D broadening model introduced in section 2 for the target heat flux density profile, see equation (5).

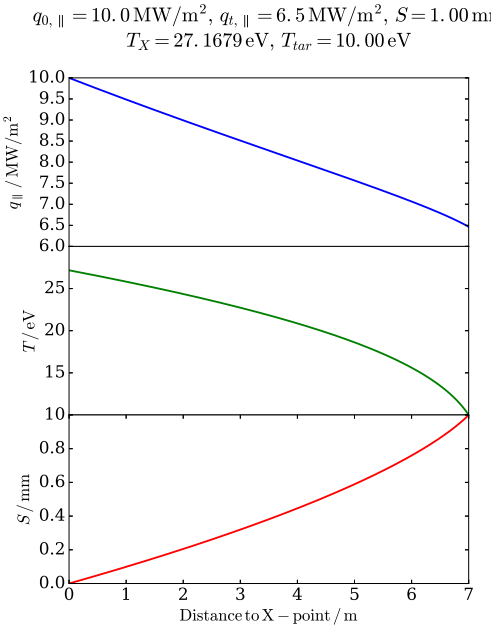

Figure 7. Parallel profiles of parallel heat flux density $q_\parallel$, electron temperature T and divertor broadening S. Perpendicular diffusivity is temperature independent ($\alpha = 0$).

A comparison of the divertor broadening S between 1D approximation and 2D calculation is shown in figure 9 for diffusivities set to yield two different S of 1 and 2 mm for $T_t = 0$ in the 2D simulation. The upper graph shows the value of S for varying target temperature. Parameters like λ_q and S are obtained from the 2D simulation by performing a least-squares fit of equation (5) to the target heat flux profile of the simulation. An example of the simulated target heat flux profile and resulting fit function

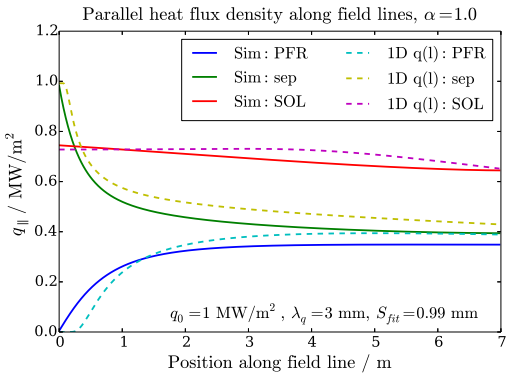

Figure 8. Heat flux density along three field lines from the 2D simulation in comparison to the Eich-model assuming a linear dependence of S to l. Simulation results are shown as solid lines, 1D approximations as dashed lines.

is shown in figure 6. The lower graph of figure 9 shows the ratio of the fitted 2D data to the 1D integral result. The approximation based on (32) underestimates S at around 25% compared to the 2D calculation, but agrees with the trend. As introduced in section 3 parameter choice $\alpha = 0$ is considered closest to experimental findings and therefore used in this comparison. Figure 10 shows the trends of 2D and 1D results for S for the case $\alpha = 0$. The values for S_{1D} were scaled with a constant according to a least-squares fit to match the values from the 2D simulation.

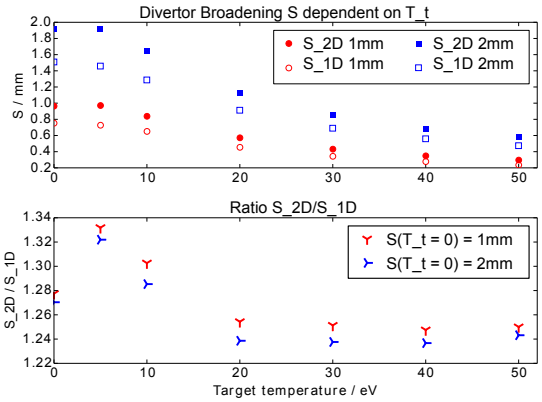

Figure 9. Ratio of S from 2D Simulation to 1D integral for constant parallel heat flux density $q = q_0 = 1\,\mathrm{MW\,m^{-2}}$. $\alpha = 0$. Note that the same ratio for the diffusivities is used for each temperature scan.

Figure 11 shows experimental and simulated values from [1] for $S = \frac{S_{tar}}{f_x}$ based on the value S_{tar} measured on the target. Shown are measured data from JET and AUG. The parameters are obtained via a least-squares fit from equation (5). In the experiment radiation from the plasma leads to additional heating of the target plates. This results in a background, that is assumed to be constant and enters as an additional constant background q_{BG} in equation (5). In SOLPS typically only heating by electrons and ions reaching the sheath is taken into account, corrected for the reflected ratio of

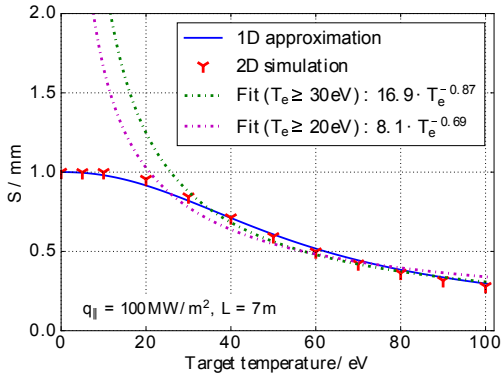

Figure 10. Best fit of inverse power law to describe S based on T_t for $T_t \geq 30\,\mathrm{eV}$ and $T_t \geq 20\,\mathrm{eV}$, $\alpha = 0$. The inverse power law reproduces S for temperatures restricted to above 20 to 30 eV.

ions. Interaction with neutrals and volume radiation are neglected. Numerical tools like SOLPS basically would basically allow to make a distinction of these heat sources for better comparison to the experiment. The regression – plotted as red line – uses only data from SOLPS simulations. The best fit for a power law is given by

$$S = (2.3 \pm 0.2) T_e^{-0.36 \pm 0.03} \ . \tag{46}$$

A regression with the same model to the 2D simulation results for temperatures starting from 30 eV the analytic function and the corresponding 2D simulation yields an exponent of -0.87, shown in figure 10. Including temperatures down to 20 eV lowers to exponent to -0.69. The scaling factor is not of interest, as a specific ratio of diffusivities leading to $S = 1\,\mathrm{mm}$ for $T_t = 0$ is used. Restricting the fit to higher target temperatures, the exponent for the temperature approaches -1.25. This is expected from equation (42) for a flat temperature profile with $T(l) \approx const$ from target to X-point.

This deviation in the exponent for higher temperatures probably is connected to a simple resolution limit. A lower limit for S is the spatial resolution of the profiles, which is about 1.7 mm on the target for the experimental data in figure 11– reference [14] from [1] –, corresponding to 0.34 mm upstream for a flux expansion of 5. The AUG L-mode data lie at that lower limit for temperatures around 40 eV and are consistently below the SOLPS fit. In addition vibrations of the camera or other optical systems as well as imperfections in the heat flux density deduction from temperature data are candidates for an overestimation of S due to additional broadening of the profiles. In the SOLPS data base the relevant heat flux density pattern is described by about 5-10 flux tubes, potentially also limiting the lower limit of S that is resolvable by the fit. The 2D simulation use radial resolutions below 0.1mm at the mid-plane. Analysis of experimental data with higher target resolutions at AUG – a factor 3 compared to the data behind [1] – find S values down to 0.2 mm and evidence for $-5/4$ being the correct exponent [2] as expected from the 1D approximation and 2D simulation for high temperatures.

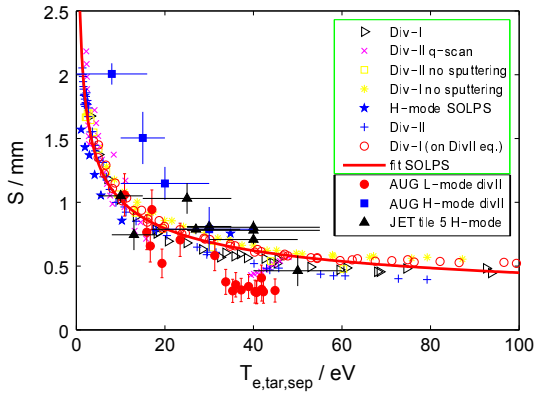

Figure 11. S as function of target electron temperature at the separatrix $T_{e,tar,sep}$, based on [1]. Red line corresponds to fit with optimal parameters $S = (2.3 \pm 0.2)T_e^{-0.36\pm0.03}$. Only the last three elements in the legend – in the black box - are measurements from the machines ASDEX Upgrade (AUG) and JET. The others – in the green box – correspond to SOLPS calculations for various Divertor configurations contributing to the fit resulting in the red line called *fit SOLPS*.

The different behaviour of S for low temperatures in figures 11 and 10 is due to different levels of physics in the models. The 1D approximation and 2D simulation are conserving energy, allowing only for perpendicular broadening. In experiments and more sophisticated simulations like SOLPS, other processes like radiation reduce the power reaching the target and thereby lead to an increase of S when performing a regression function (5) on the target heat flux profiles profiles. Another process is heating of the target by radiation, which leads to larger values of S for reduced peak power loads by plasma transport.

6. Interpretation

An 1D approximation for the divertor broadening S is found by integrating the temperature profile along the separatrix between X-point and divertor target. While a power law scaling for T_t is valid for high target temperatures, this is not true for low target temperatures due to the strong parallel temperature gradient. This approach implies, that it is not enough to reduce the plasma temperature close to the target for larger machines like ITER and DEMO to achieve the required low target heat flux, but the temperature has to be lowered in a large volume in front of the target. This could be achieved by e.g. radiation or charge exchange in the divertor volume.

Also a faster decrease of S with high temperatures is expected from the 1D approximation and simple 2D simulation, as SOLPS and experiments operate at the resolution limit in terms of deducing S. For a discussion of data with higher target resolution – finding $S \propto T_{e,target}^{-5/4}$ – see [2]. As it turns out, the gyro-radius has to be taken into account, when it get's comparable with the perpendicular transport broadening. This is not taken into account by the 1D approximation or 2D simulation presented in

this work.

An important consequence is, that an increase of the length of the divertor leg – in which conduction is the dominant transport parameter – will increase the divertor broadening less than linear – as suggested by (2) – due to the strong temperature gradient in front of the target and therefore an almost unchanged high temperature near the X-point with low contribution to S. Additional connection length, however, can be used to decrease the parallel heat flux density in the divertor volume by radiation and dissipative processes, so that the temperature gradient in front of the target is lowered, which leads to an increase of S.

The presented 1D analysis neglects processes like convective transport, drifts and radiation, which limits the predictive capability of the approximation, as these are known to have an influence on the target heat flux profile. The 2D simulation used for comparison assumes a constant pressure in the divertor volume and a homogeneous target temperature for better comparability. Both neglect the influence of neutral particles, known to be important for detachment, reducing heat and particle flux to the target.

Therefore the presented approximation delivers an approximation for attached conditions, with conduction being the dominating transport in the divertor volume. Using the formulation introduced in this paper, an integration for arbitrary dependencies of the diffusivities on n and T can be done numerically with little effort to find a better suited 1D approximation. The simulation can also be seen as prediction for the broadening due to perpendicular transport. In addition radiation and other processes can lead to a broadening.

When analysing target heat flux density profiles, one must distinguish two mechanisms altering its shape from the X-point to the target. Perpendicular broadening describes an energy conserving process, which is thought to be represented by S and is due to an-isotropic heat transport. On the other hand losses like radiation, charge exchange etc remove heat from the plasma by other means than convective or conductive transport. They lead to a flattening of the peak heat flux – mimicking perpendicular broadening – and affect the deduction of transport parameters from the heat flux profiles. These losses can lead to an overestimation of S also in simulations with codes like SOLPS – with respect to the value of S associated with pure energy conserving perpendicular broadening.

7. Conclusions

It is shown that for pure conductive transport in the divertor region a power law of the divertor broadening S to the target electron temperature T_t as the suggested in [1] is only valid for temperatures T_t above about 20 eV. The further increase of S for lower target temperatures in experiments and SOLPS simulations seems to be driven by heat loss processes like radiation, not conduction. This raises the question, whether

the common analysis, using a single broadening parameter S, to explain the smoothness of the profiles – seen as a reduction of the peak heat flux – as deviation from a pure truncated exponential decay is enough.

However, for decreasing target temperatures ($T_t < 20\,\mathrm{eV}$) the increase of S stagnates and the conductive 1D approximation results in a finite value of S even for zero target temperature.

It is concluded that the target temperature is not a valid parameter for a power law scaling, as it is not representative for the entire divertor volume due to the increasing temperature gradients with decreasing temperature. This is shown in simulations solving the 2D heat diffusion equation, which is used as reference for an analytic 1D approximation describing the divertor broadening along a field line solely by the ratio of the perpendicular to the parallel diffusivity. To solve this a distinction between the *conductive* S – for perpendicular broadening – and an effective broadening S_{eff} to include heat losses is suggested.

8. Acknowledgment

This work has been carried out within the framework of the EUROfusion Consortium and has received funding from the Euratom research and training programme 2014-2018 under grant agreement No 633053. The views and opinions expressed herein do not necessarily reflect those of the European Commission.

References

[1] A. Scarabosio et al. “Scaling of the divertor power spreading (S-factor) in open and closed divertor operation in JET and ASDEX Upgrade”. In: *Journal of Nuclear Materials* 463 (2015). PLASMA-SURFACE INTERACTIONS 21, pp. 49–54. ISSN: 0022-3115. DOI: 10.1016/j.jnucmat.2014.11.076. URL: http://www.sciencedirect.com/science/article/pii/S0022311514008794.

[2] B Sieglin et al. “Investigation of scrape-off layer and divertor heat transport in ASDEX Upgrade L-mode”. In: *Plasma Physics and Controlled Fusion* 58.5 (2016), p. 055015. URL: http://stacks.iop.org/0741-3335/58/i=5/a=055015.

[3] T. Eich et al. “Scaling of the tokamak near the scrape-off layer H-mode power width and implications for ITER”. In: *Nuclear Fusion* 53.9 (2013), p. 093031. URL: http://stacks.iop.org/0029-5515/53/i=9/a=093031.

[4] P.C. Stangeby. *The Plasma Boundary of Magnetic Fusion Devices*. Series in Plasma Physics and Fluid Dynamics. Taylor & Francis, 2000. ISBN: 9780750305594.

[5] M. A. Makowski et al. “Analysis of a multi-machine database on divertor heat fluxes)”. In: *Physics of Plasmas* 19.5, 056122 (2012). DOI: http://dx.doi.org/10.1063/1.4710517. URL: http://scitation.aip.org/content/aip/journal/pop/19/5/10.1063/1.4710517.

[6] B Sieglin et al. "Power load studies in JET and ASDEX-Upgrade with full-W divertors". In: *Plasma Physics and Controlled Fusion* 55.12 (2013), p. 124039. URL: http://stacks.iop.org/0741-3335/55/i=12/a=124039.

[7] S. Wiesen et al. "The new SOLPS-ITER code package". In: *Journal of Nuclear Materials* 463 (2015). PLASMA-SURFACE INTERACTIONS 21, pp. 480–484. ISSN: 0022-3115. DOI: https://doi.org/10.1016/j.jnucmat.2014.10.012. URL: http://www.sciencedirect.com/science/article/pii/S0022311514006965.

[8] Xavier BONNIN et al. "Presentation of the New SOLPS-ITER Code Package for Tokamak Plasma Edge Modelling". In: *Plasma and Fusion Research* 11 (2016), pp. 1403102–1403102. DOI: 10.1585/pfr.11.1403102.

[9] M Faitsch et al. "Change of the scrape-off layer power width with the toroidal B-field direction in ASDEX upgrade". In: *Plasma Physics and Controlled Fusion* 57.7 (2015), p. 075005. URL: http://stacks.iop.org/0741-3335/57/i=7/a=075005.

[10] B.K. Venkanna. *Fundamentals of Heat and Mass Transfer*. ISBN 9788120340312. Prentice-Hall Of India Pvt. Limited.

[11] David Bohm. "The characteristics of electrical discharges in magnetic fields". In: *New York: McGraw-Hill* (1949).

[12] William H. Press et al. *Numerical Recipes*. third edition. Cambridge University Press, 2007.

[13] J. A. Bittencourt. *Fundamentals of Plasma Physics*. Third. Fundamentals of Plasma Physics, Third Edition by J.A. Bittencourt. Published by Springer-Verlag, New York, Inc.; 2004. ISBN 0-387-20975-1., 2004.

[14] T. Eich et al. "Inter-ELM Power Decay Length for JET and ASDEX Upgrade: Measurement and Comparison with Heuristic Drift-Based Model". In: *Phys. Rev. Lett.* 107 (21 Nov. 2011), p. 215001. DOI: 10.1103/PhysRevLett.107.215001. URL: https://link.aps.org/doi/10.1103/PhysRevLett.107.215001.